Bi-layered coded metasurface for multi-functional hologram with broadband transmission and efficient reflection

Lei Zhu (朱 磊)[1,2,3*], Xusheng Li (李绪胜)[2], Liang Dong (董 亮)[2], Wenjing Xie (谢文静)[2], Guanyu Shang (尚关玉)[4], Shah Nawaz Burokur[5***], and Xumin Ding (丁旭旻)[6,7**]

[1] School of Computer and Control Engineering, Qiqihar University, Qiqihar 161006, China
[2] Communication and Electronics Engineering Institute, Qiqihar University, Qiqihar 161006, China
[3] Heilongjiang Key Laboratory of Big Data Network Security Detection and Analysis, Qiqihar University, Qiqihar 161000, China
[4] Department of Microwave Engineering, Harbin Institute of Technology, Harbin 150001, China
[5] LEME, UPL, Université Paris Nanterre, F92410 Ville d'Avray, France
[6] Advanced Microscopy and Instrumentation Research Center, Harbin Institute of Technology, Harbin 150080, China
[7] Key Laboratory of Millimeter Waves, Southeast University, Nanjing 210096, China

*Corresponding author: zhulei@qqhru.edu.cn
**Corresponding author: xuminding@hit.edu.cn
***Corresponding author: sburokur@parisnanterre.fr
Received November 27, 2023 | Accepted January 26, 2024 | Posted Online May 17, 2024

A multi-functional full-space metasurface based on frequency and polarization multiplexing is proposed. The metasurface unit consists of metallic patterns printed on the two faces of a single-layered dielectric substrate. The unit cell can control electromagnetic wavefronts to achieve a broadband transmission with amplitudes greater than 0.4 from 4.4 to 10.4 GHz. Meanwhile, at 11.7 GHz and 15.4 GHz, four high-efficiency reflection channels with a reflection amplitude greater than 0.8 are also realized. When illuminated by linearly polarized waves, five different functions can be realized at five different frequencies, which are demonstrated by theoretical calculations, full-wave simulations, and experimental measurements.

1. Introduction

In the field of wireless communications, it is crucial to be able to manipulate electromagnetic wavefronts. Therefore, metasurfaces with the ability to control electromagnetic wavefronts have attracted extensive attention. As the two-dimensional counterpart of metamaterials[1], metasurfaces circumvent the issues related to high loss and complex fabrication and allow the precise control of the amplitude[2–4], phase[5], and polarization[6] of electromagnetic waves, opening the door to interesting prospects. At present, metasurfaces have been proposed for a wide range of applications, such as perfect lens[7], vortex beams[8], camouflaging[9], and image holograms[10–15].

So far, metasurface holograms have achieved rapid developments due to their applications in information encryptions and imaging displays[16,17]. At present, metasurface holograms are mainly divided into reflective metasurface holograms[18] and transmissive metasurface holograms[19]. These two kinds of

metasurfaces have powerful abilities to manipulate electromagnetic waves in only semi-space but limit the utilization of space resources. To improve the utilization of space resources and increase information capacity, full-space metasurfaces have been proposed in recent years[20–24]. For example, Wu et al. proposed a multi-band bidirectional full-space metasurface, which can realize different functions in six frequency bands[21]. However, the metasurface adopts a multi-layered configuration, which results in a complex structure with high manufacturing costs. In addition, the accuracy of the fabrication is significantly affected by the precision of the assembly of the multi-layered structure.

To solve the multi-layered substrate problem of the full-space metasurface, Xie et al. proposed a full-space metasurface with a single-layered substrate[22]. The metasurface enables the generation of holograms in the reflection space and the generation of four-vortex beams in the transmission space for the circularly polarized wave illuminations. However, this metasurface only realizes two independent functions, which limits the

information capacity and does not align with the trend of highly integrated electronic devices. Moreover, the previously reported metasurface holograms show narrow bandwidth features, while broadband metasurface may expand the application boundaries of imaging technologies even further. Therefore, it is still a challenge to realize a multi-functional and full-space metasurface with broadband characteristics using a single-layered substrate.

Here, a full-space 1-bit coding metasurface enabling five functionalities is proposed, which can independently control the reflected and transmitted electromagnetic waves at different frequencies to realize different functions. The metasurface is constructed from a coding unit that presents a high phase modulation ability for linearly polarized waves. By judiciously designing the unit structure, there is no crosstalk between channels, which is beneficial for multi-functional phase modulation. Based on the principle of transmission phase, the reflection modes of the x- and y-polarized waves can be tailored by changing the structural parameters of the metal patterns. At the same time, according to the principle of geometric phase, the x-polarized waves can be manipulated by rotating the metal structure on the substrate for the transmission mode. A proof-of-concept full-space 1-bit coding metasurface prototype with five independent functions is designed and fabricated. The different functions are verified by full-wave simulations and validated by experimental measurements, exhibiting single-focus, transverse and vertical double-focus, and "T" and "J" alphabet images. This work presents an effective way to improve the information capacity of the metasurface and solve the complex structure problem of the multi-functional metasurface.

2. Design of the Coding Elements

Figure 1 shows the schematic diagram of the proposed multi-functional full-space 1-bit coding metasurface. When an x-polarized electromagnetic wave illuminates the metasurface, a single focus image is reconstructed in the transmission space over a broad frequency range, noted as f_1, while the "J" letter and vertical bifocal images are produced in the reflection space at frequencies f_2 and f_3, respectively. Similarly, when a y-polarized electromagnetic wave illuminates the metasurface, the "T" letter and horizontal bifocal images are reconstructed in the reflection space at frequencies f_2 and f_3, respectively.

The design of the coding unit is crucial for realizing the multi-functional full-space coding metasurface hologram displayed in Fig. 1. In order to achieve phase modulation of electromagnetic waves in the whole space, a coding unit cell with high efficiency and high isolation is designed. Under incident linearly-polarized (LP) electromagnetic waves, the reflection and transmission characteristics of the coding unit are described as

$$R = \begin{pmatrix} r_{xx}e^{i\varphi_x^r} & 0 \\ 0 & r_{yy}e^{i\varphi_y^r} \end{pmatrix}, \tag{1}$$

$$T = \begin{pmatrix} 0 & t_{xy}e^{i\varphi_{xy}^t} \\ 0 & 0 \end{pmatrix}, \tag{2}$$
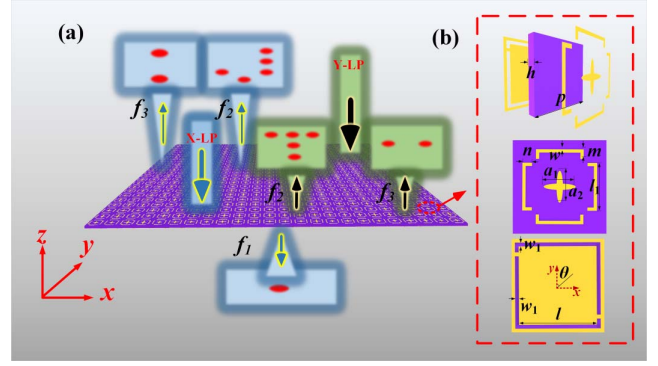

Fig. 1. (a) Schematic diagram of the proposed five-function full-space metasurface. (b) Schematic diagram of the coding element, where perspective, top and bottom views are shown.

where r_{xx} and r_{yy} represent the co-polarized reflection amplitudes under x- and y-polarized waves illuminations, respectively, and t_{xy} represents the cross-polarized transmission amplitude under x-polarized waves illumination. φ_x, φ_y, and φ_{xy} are the corresponding phase shifts. To achieve perfect reflection under the LP incidence (i.e., $|r_{xx}| = 1$, $|r_{yy}| = 1$), the phase shifts φ_x and φ_y can be arbitrarily modulated by altering the structural parameters of the coding unit. Similarly, the cross-polarized transmission phase shift φ_{xy} can be effectively adjusted by modulating the rotation angle of the coding unit.

Based on the above analysis, a coding element owning different characteristics in different frequency bands is designed, as illustrated in Fig. 1(b). According to the Jones matrix theory in Eqs. (1) and (2), based on the propagation and geometric phase principles, by changing the geometric dimensions and the in-plane rotation angles of each sub-element, highly efficient phase control can be achieved. The top face of the metasurface element consists of an oval cross-patch and half I-shaped rod structures, while the bottom face includes a metal ground plane with rectangular gaps. The metal material on the top and bottom layers is copper with a thickness of 0.018 mm. The relative permittivity and loss tangent of the dielectric substrate with thickness $h = 1\,\text{mm}$ are $\varepsilon_r = 3.5$ and $\tan\delta = 0.001$. The other parameters of the metasurface element are $p = 12\,\text{mm}$, $w = 0.4\,\text{mm}$, $w_1 = 0.5\,\text{mm}$, $l = 10\,\text{mm}$, and $l_1 = 6\,\text{mm}$. The proposed coding unit owns the full-space wavefront control capability. To highlight the reflection and transmission performances of the coding unit under the x- and y-polarized incident waves, simulations using the CST Microwave Studio commercial software are performed, where periodic boundary conditions are applied to an elementary unit in the x- and y-directions to simulate an infinite array.

Figure 2 shows the simulation results for the metasurface constitutive element. Under an x-polarized incident wave illumination, the transmission amplitude and phase of the coding elements vary with θ, as shown in Fig. 2(a). The amplitude of the cross-polarized transmitted wave is above 0.4 from 4.4 to 10.4 GHz, which approaches the theoretical limit of 0.5[23]. Meanwhile, based on the geometric phase principle, by adjusting
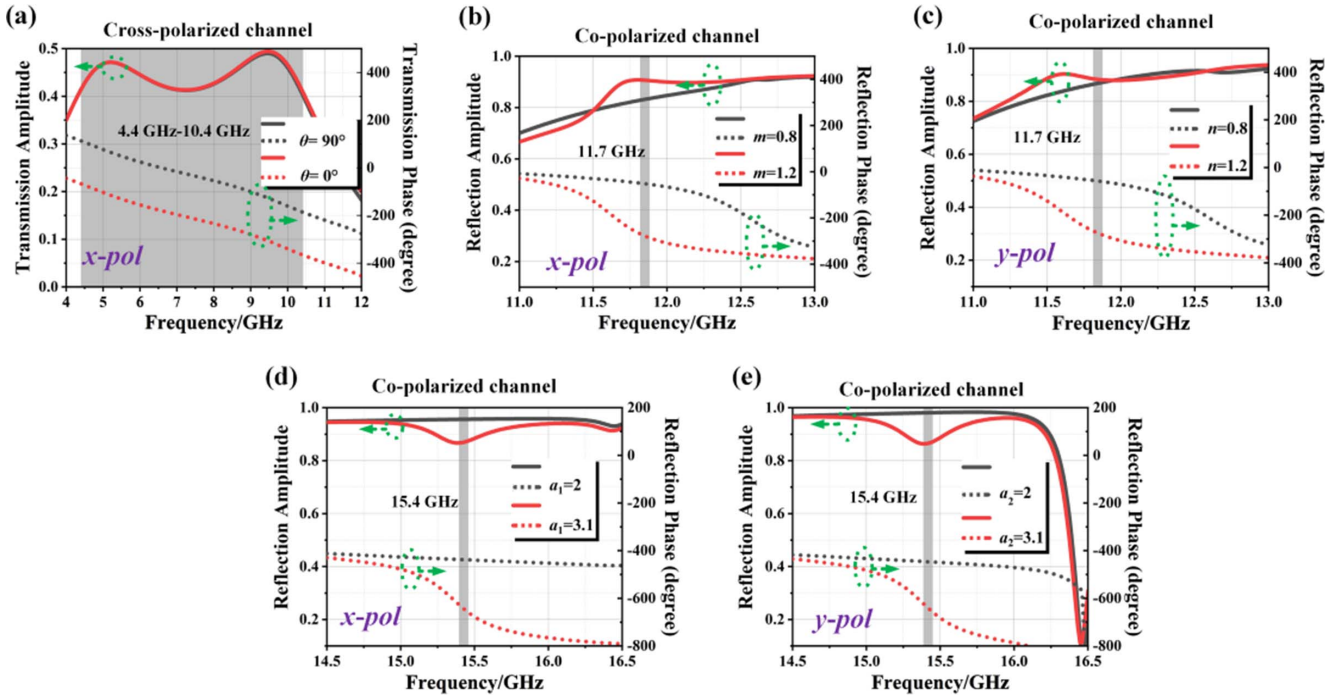
Fig. 2. Amplitude and phase characteristics of the coding unit cell. (a) Cross-polarized transmission amplitude and phase under the *x*-polarized wave incidence. (b), (c) Co-polarized reflection amplitude and phase under the *x*- and *y*-polarized wave incidences, respectively, for operation at 11.7 GHz. (d), (e) Co-polarized reflection amplitude and phase under the *x*- and *y*-polarized wave incidences, respectively, for operation at 15.4 GHz. The values of *m*, *n*, a_1, and a_2 are given in mm.

the rotation angle θ of the slit, the unit cell exhibits a phase shift of 180° in the wide frequency range, which is able to achieve 1-bit transmission phase coding. Moreover, the proposed unit exhibits broadband transmission characteristics, which results from the excitation of multiple resonant modes of the metal structure[25]. On the other hand, based on the transmission phase principle, by adjusting the size of the half I-shaped structures (oval cross-patch) on the top layer, specifically by changing the value of the variable *m* (a_1), the *x*-polarized wave can be manipulated in the reflective space at 11.7 GHz (15.4 GHz). The simulation results, presented in Figs. 2(b) and 2(d), demonstrate that the reflection amplitudes are greater than 0.8, and the phase difference is about 180°, enabling the 1-bit phase coding mechanism. Similarly, under the *y*-polarized electromagnetic wave incidence, by changing the value of the variable *n* (a_2), 1-bit phase coding can also be realized at 11.7 GHz and 15.4 GHz, as illustrated in Figs. 2(c) and 2(e). The detailed structural parameters of the coding units composing the metasurface are shown in Table 1, where the horizontal data represent the digital encoding of the two channels under the *y*-polarized wave illumination. Among them, 0/0 represents the digital code at 11.7 GHz and 15.4 GHz, with the digital states of 0 and 1 standing for transmission phases of 0° and 180°, respectively. The vertical data represent the digital encoding of the three channels under the *x*-polarized wave illumination. Meanwhile, 0/0/0 represents the digital code at 4.4 GHz–10.4 GHz, 11.7 GHz, and 15.4 GHz, where the digital states of 0 and 1 stand for transmission phases of 0° and 180°, respectively.

Figure 3 shows the instantaneous induced surface current distributions of the top and bottom layers of the unit cell for illuminations by *x*- and *y*-polarized waves. At 8 GHz, when the *x*-polarized wave illuminates the unit cell, the current is mainly concentrated on the bottom metal frame structure, while the top structure barely responds, as shown in Fig. 3(a). Figures 3(c) and 3(e) show that under the incidence of *x*-polarized waves, strong resonances occur only along the *x*-direction in the half I-shaped and oval cross-patch structures at 11.7 GHz and 15.4 GHz, respectively. Other metallic parts of the coding unit cell almost show only slight electromagnetic responses. Therefore, the phase responses of the *x*-polarized reflected waves at 11.7 GHz and 15.4 GHz are primarily influenced by two key factors: the half I-shaped structure along the *x*-direction and the elliptical structure along the *x*-direction in the elliptical cross-patch. Similarly, the phase responses of the *y*-polarized waves mainly depend on the *y*-direction in the half-I-shaped and oval cross-patch structures, as shown in Figs. 3(b) and 3(d). Through the above analysis, it can be found that when one of the five resonators is changed, the electromagnetic characteristics of other resonators would be negligibly affected. Therefore, the metasurface element can greatly reduce the crosstalk between different resonators, achieving independent control of the corresponding incident waves.

3. Design of Metasurface Hologram

To further verify the effectiveness of full-space EM wavefront manipulation, the aforementioned meta-atoms are arranged

in an array to form the phase-encoded metasurface, which contains five different encoding modes to realize five independent channels at different frequencies. In this research, a 24×24 array of units is employed to construct a metasurface holographic array, which has been thoughtfully designed using the weighted Gerchberg-Saxton (GSW) algorithm[26]. Full-wave

Table 1. Detailed Structural Parameters Corresponding to the Encoding Units of the Metasurface.

x pol	*y* pol			
	0/0 11.7 GHz/15.4 GHz	0/1 11.7 GHz/15.4 GHz	1/0 11.7 GHz/15.4 GHz	1/1 11.7 GHz/15.4 GHz
0/0/0 4.4–10.4 GHz/11.7 GHz/15.4 GHz	$\theta = 0°$	$\theta = 0°$	$\theta = 0°$	$\theta = 0°$
	$m = 1.2$ mm	$m = 1.2$ mm	$m = 1.2$ mm	$m = 1.2$ mm
	$a_1 = 3.1$ mm	$a_1 = 3.1$ mm	$a_1 = 3.1$ mm	$a_1 = 3.1$ mm
	$n = 1.2$ mm	$n = 1.2$ mm	$n = 0.8$ mm	$n = 0.8$ mm
	$a_2 = 3.1$ mm	$a_2 = 2$ mm	$a_2 = 3.1$ mm	$a_2 = 2$ mm
0/0/1 4.4–10.4 GHz/11.7 GHz/15.4 GHz	$\theta = 0°$	$\theta = 0°$	$\theta = 0°$	$\theta = 0°$
	$m = 1.2$ mm	$m = 1.2$ mm	$m = 1.2$ mm	$m = 1.2$ mm
	$a_1 = 2$ mm	$a_1 = 2$ mm	$a_1 = 2$ mm	$a_1 = 2$ mm
	$n = 1.2$ mm	$n = 1.2$ mm	$n = 0.8$ mm	$n = 0.8$ mm
	$a_2 = 3.1$ mm	$a_2 = 2$ mm	$a_2 = 3.1$ mm	$a_2 = 2$ mm
0/1/0 4.4–10.4 GHz/11.7 GHz/15.4 GHz	$\theta = 0°$	$\theta = 0°$	$\theta = 0°$	$\theta = 0°$
	$m = 0.8$ mm	$m = 0.8$ mm	$m = 0.8$ mm	$m = 0.8$ mm
	$a_1 = 3.1$ mm	$a_1 = 3.1$ mm	$a_1 = 3.1$ mm	$a_1 = 3.1$ mm
	$n = 1.2$ mm	$n = 1.2$ mm	$n = 0.8$ mm	$n = 0.8$ mm
	$a_2 = 3.1$ mm	$a_2 = 2$ mm	$a_2 = 3.1$ mm	$a_2 = 2$ mm
0/1/1 4.4–10.4 GHz/11.7 GHz/15.4 GHz	$\theta = 0°$	$\theta = 0°$	$\theta = 0°$	$\theta = 0°$
	$m = 0.8$ mm	$m = 0.8$ mm	$m = 0.8$ mm	$m = 0.8$ mm
	$a_1 = 2$ mm	$a_1 = 2$ mm	$a_1 = 2$ mm	$a_1 = 2$ mm
	$n = 1.2$ mm	$n = 1.2$ mm	$n = 0.8$ mm	$n = 0.8$ mm
	$a_2 = 3.1$ mm	$a_2 = 2$ mm	$a_2 = 3.1$ mm	$a_2 = 2$ mm
1/0/0 4.4–10.4 GHz/11.7 GHz/15.4 GHz	$\theta = 90°$	$\theta = 90°$	$\theta = 90°$	$\theta = 90°$
	$m = 1.2$ mm	$m = 1.2$ mm	$m = 1.2$ mm	$m = 1.2$ mm
	$a_1 = 3.1$ mm	$a_1 = 3.1$ mm	$a_1 = 3.1$ mm	$a_1 = 3.1$ mm
	$n = 1.2$ mm	$n = 1.2$ mm	$n = 0.8$ mm	$n = 0.8$ mm
	$a_2 = 3.1$ mm	$a_2 = 2$ mm	$a_2 = 3.1$ mm	$a_2 = 2$ mm
1/0/1 4.4–10.4 GHz/11.7 GHz/15.4 GHz	$\theta = 90°$	$\theta = 90°$	$\theta = 90°$	$\theta = 90°$
	$m = 1.2$ mm	$m = 1.2$ mm	$m = 1.2$ mm	$m = 1.2$ mm
	$a_1 = 2$ mm	$a_1 = 2$ mm	$a_1 = 2$ mm	$a_1 = 2$ mm
	$n = 1.2$ mm	$n = 1.2$ mm	$n = 0.8$ mm	$n = 0.8$ mm
	$a_2 = 3.1$ mm	$a_2 = 2$ mm	$a_2 = 3.1$ mm	$a_2 = 2$ mm

(Continued)

Table 1. (Continued)

x pol	y pol			
	0/0 11.7 GHz/15.4 GHz	0/1 11.7 GHz/15.4 GHz	1/0 11.7 GHz/15.4 GHz	1/1 11.7 GHz/15.4 GHz
1/1/0 4.4–10.4 GHz/11.7 GHz/15.4 GHz	$\theta = 90°$	$\theta = 90°$	$\theta = 90°$	$\theta = 90°$
	$m = 0.8$ mm	$m = 0.8$ mm	$m = 0.8$ mm	$m = 0.8$ mm
	$a_1 = 3.1$ mm	$a_1 = 3.1$ mm	$a_1 = 3.1$ mm	$a_1 = 3.1$ mm
	$n = 1.2$ mm	$n = 1.2$ mm	$n = 0.8$ mm	$n = 0.8$ mm
	$a_2 = 3.1$ mm	$a_2 = 2$ mm	$a_2 = 3.1$ mm	$a_2 = 2$ mm
1/1/1 4.4–10.4 GHz/11.7 GHz/15.4 GHz	$\theta = 90°$	$\theta = 90°$	$\theta = 90°$	$\theta = 90°$
	$m = 0.8$ mm	$m = 0.8$ mm	$m = 0.8$ mm	$m = 0.8$ mm
	$a_1 = 2$ mm	$a_1 = 2$ mm	$a_1 = 2$ mm	$a_1 = 2$ mm
	$n = 1.2$ mm	$n = 1.2$ mm	$n = 0.8$ mm	$n = 0.8$ mm
	$a_2 = 3.1$ mm	$a_2 = 2$ mm	$a_2 = 3.1$ mm	$a_2 = 2$ mm

simulations are carried out, where linearly polarized plane waves are used as the excitation source. The designed operating frequencies are 4.4–10.4 GHz, 11.7 GHz, and 15.4 GHz, and the electromagnetic simulation results are shown in Figs. 4 and 5. For the transmission mode, when the metasurface is illuminated by an x-polarized wave, the theoretically calculated image is shown in Fig. 4(b). To verify the broadband feature of the transmissive holographic imaging within the 4.4–10.4 GHz frequency range, simulation results are also shown at 4.7 GHz, 6 GHz, 8 GHz, and 10.4 GHz at focusing distances 60 mm, 80 mm, 120 mm and 185 mm, respectively. The simulated holographic images at these four frequencies are in good agreement with the theoretical calculation results, as shown in Figs. 4(c), 4(d), 4(e), and 4(f). In addition, the imaging efficiency, which is defined as the ratio of the energy in the image to the incident energy, is utilized to evaluate the quality of holographic images. The imaging efficiency of the single focus at the four frequencies is 23.06%, 22.24%, 19.09%, and 22.83%, indicating good imaging performances for the cross-polarized transmission channel.
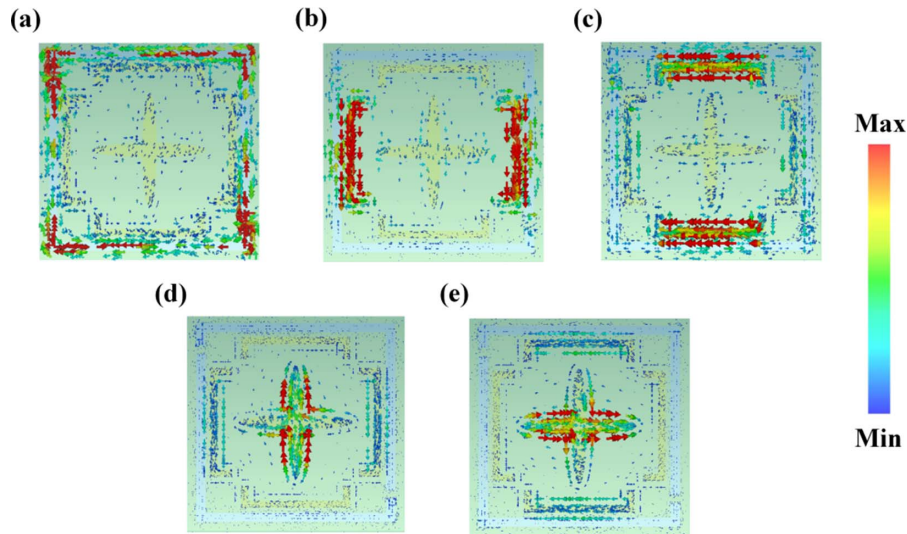

Fig. 3. Current distributions on the top and bottom layers of the unit cell. (a) At 8 GHz under x-polarized incidence. (b) At 11.7 GHz under y-polarized incidence. (c) At 11.7 GHz under x-polarized incidence. (d) At 15.4 GHz under y-polarized incidence. (e) At 15.4 GHz under x-polarized incidence.
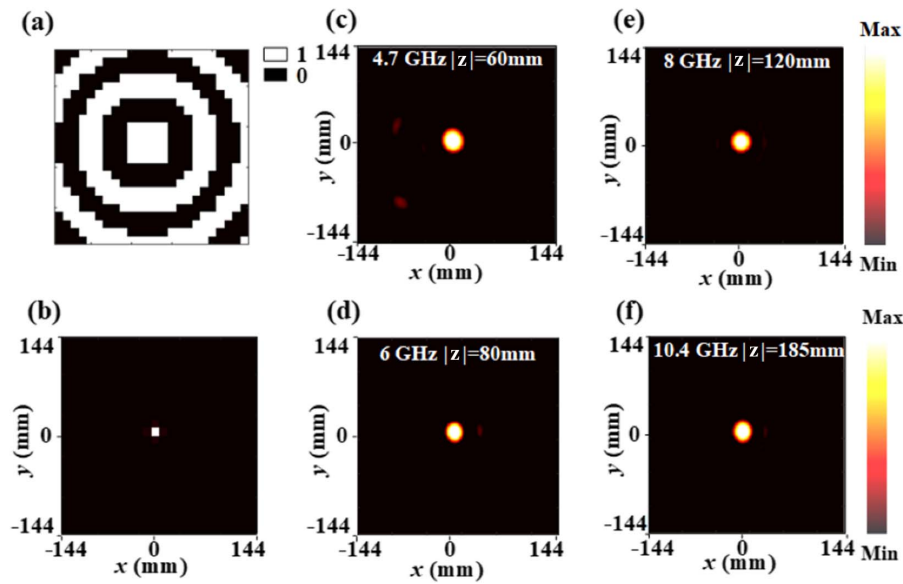
Fig. 4. (a) Coding map of cross-polarized channel in transmission mode. (b) Theoretical calculation result of the holographic image. Simulation results of imaging at (c) 4.7 GHz, (d) 6 GHz, (e) 8 GHz, and (f) 10.4 GHz.

The calculated phase maps and the theoretical and simulated images in the reflection semi-space are shown in Fig. 5. The focal planes are set as $z = 84$ mm and $z = 90$ mm at 11.7 GHz and 15.4 GHz, respectively. Under the x-polarized wave incidence, the electromagnetic reconstruction of the letter "J" and the vertical bifocal image are achieved at 11.7 GHz and 15.4 GHz, respectively, while under the y-polarized wave incidence, the letter "T" and the transverse bifocal image are realized at 11.7 GHz and 15.4 GHz, respectively. The bandwidth for each of these configurations is about 0.05 GHz. For the reflective mode, all the simulation results show good agreement with the calculations, where the imaging efficiencies of the letter "J", the vertical bifocal image, the letter "T", and horizontal bifocal image are 44.08%, 67.05%, 46.89%, and 67.58%, respectively, with good imaging features. The imaging efficiency can be further enhanced by considering different approaches, such as optimizing a meta-atom with higher degrees of freedom to decouple the coherence between amplitude and phase or discretizing the full 2π phase profile into more stages. In addition, the design of the multi-layered structure and the selection of low-loss materials can form specific electromagnetic resonance modes and enhance the transmission of electromagnetic waves at specific frequencies.

To further prove the feasibility of the multi-functional metasurface, the proposed 288 mm × 288 mm metasurface is fabricated by classical printed circuit board (PCB) technology, as illustrated by the photographs in Fig. 6(a). The schematic diagram of the experimental near-field scanning system is shown in Fig. 6(b). A quasi-plane wave, generated by a 2–18 GHz wideband horn antenna and positioned 120 cm away from the metasurface, is used to illuminate the metasurface. Then, the linearly polarized electric fields in the imaging planes are measured using an EFS-105-12 fiber optic active near-field probe with a 6.6 mm × 6.6 mm pure dielectric head. Both the horn antenna and the probe are connected to an Agilent 8722ES vector network analyzer (VNA), and the probe is moved in small increments of 2 mm in the xoy-plane to obtain a full two-dimensional spatial electric field distribution.

Figure 6(c) shows the measured results of holographic images in the transmission semi-space, in which the single focal point is clearly visible. The four holographic images at frequencies of 4.7 GHz, 6 GHz, 8 GHz, and 10.4 GHz exhibit good imaging quality. Figures 6(d)–6(g) show the four images in the reflection semi-space for the x- and y-polarized wave incidences at 11.7 GHz and 15.4 GHz. It is important to note that for the test results of the reflection mode, the final imaging results need to be post-processed, where the incident field measured without the metasurface is subtracted from the total field measured in the presence of the metasurface in order to extract only the reflected field.

In summary, the test results are consistent with the theoretical and simulation results and demonstrate that the designed coding metasurface can focus electromagnetic wave energy to the target area for obtaining high-quality holographic images. It is worth noting that the test results in the reflective mode are slightly different from the simulation results shown in Fig. 5. The factors that affect the imaging performances may include the following aspects. The first factor is manufacturing errors, followed by the difference between the ideal plane wave used in simulations and the quasi-plane wave used in the experiments. Additionally, a slight off-axis deviation of the horn antenna can also affect the imaging quality. To improve the imaging performance, enhancing the machining accuracy of the metasurface and minimizing machining errors can be considered. Moreover, using a Gaussian beam horn antenna can bring the incident electromagnetic wave closer to an ideal plane wave,
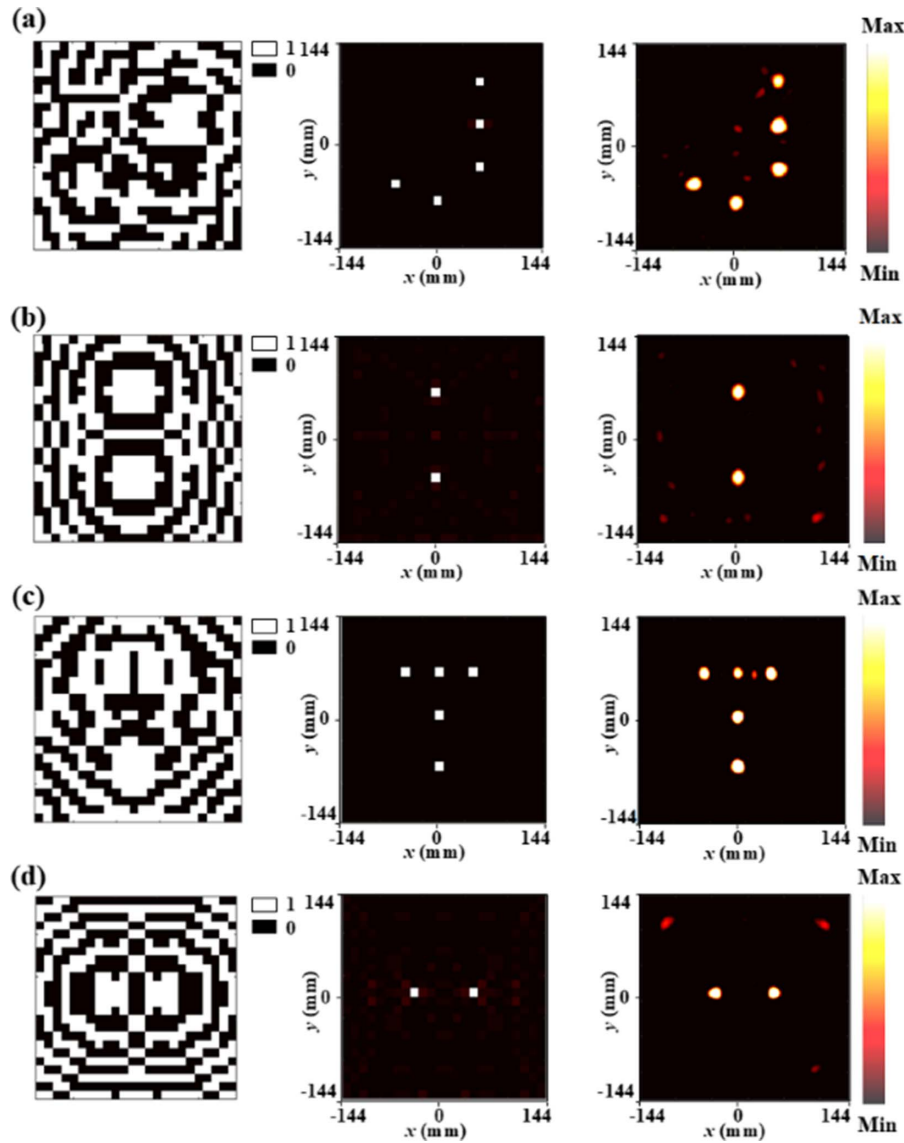
Fig. 5. Phase coding map, theoretical calculation results and simulation results of the different images in the reflection semi-space. (a) "J" hologram. (b) Vertical bifocal image. (c) "T" hologram. (d) Horizontal bifocal image.

while ensuring correct alignment of the horn antenna and the metasurface.

4. Conclusion

In conclusion, a full-space multi-functional metasurface designed using a bi-layered copper-cladded single dielectric substrate is proposed to operate under linearly polarized electromagnetic wave incidences. The top metal layer consists of half I-shaped and oval cross-patches, which are used to modulate the reflected electromagnetic wavefront at 11.7 GHz and 15.4 GHz, respectively. The bottom metal layer is used to modulate the transmitted spatial wavefront in the 4.4–10.4 GHz frequency band. Based on the transmission phase and geometric phase principles, the independent electromagnetic modulation between each channel is realized by modulating the dimensions of the unit cell structure. As an example, a designed five-function full-space metasurface has been simulated, and its performances have been verified experimentally. Five holographic images are reconstructed at specific operating frequencies, with a good agreement among experiments, numerical predictions, and full-wave simulations. The proposed full-space metasurface has a strong ability to manipulate the reflection and broadband transmission properties of electromagnetic waves using a single-layered patterned substrate. Such metasurfaces can provide multiple degrees of freedom for electromagnetic wave manipulation, improve the information capacity of the metasurface, and pave the way for advanced communication multi-functional devices.
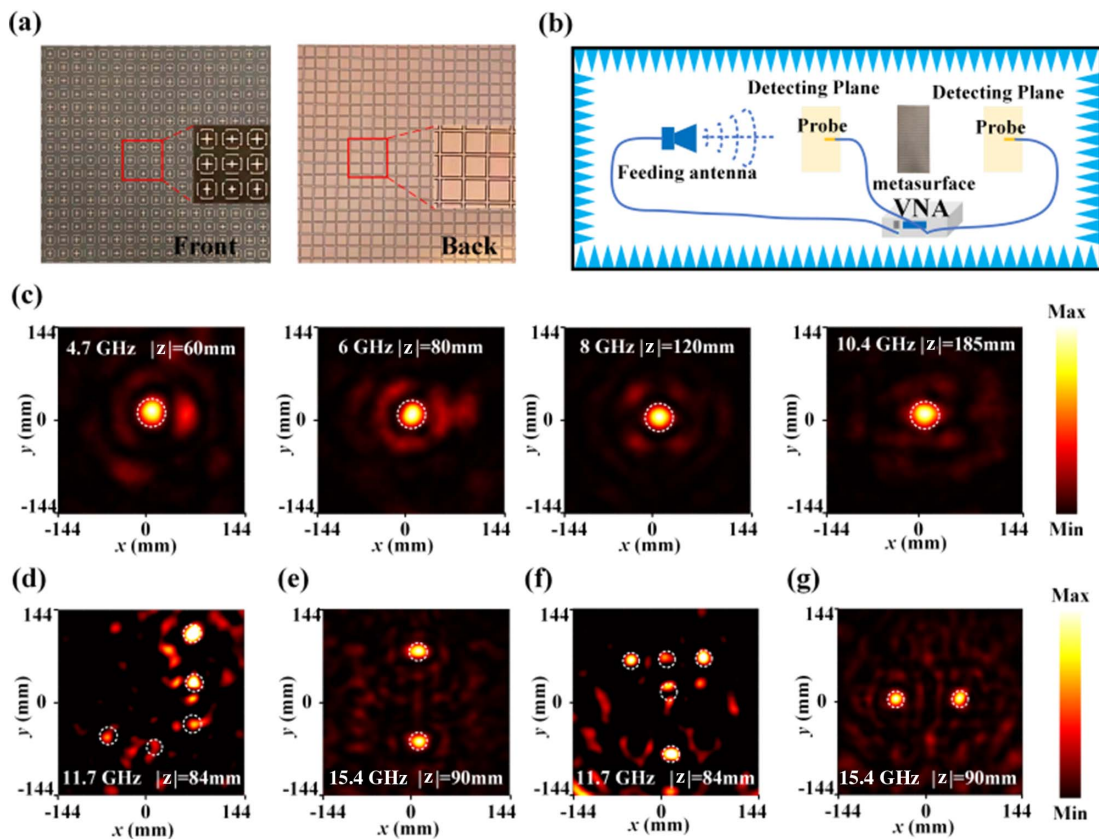
Fig. 6. (a) Photographs of the front and back faces of the fabricated metasurface sample. (b) Illustration of the experimental setup used to scan the electric field in the imaging plane. (c) Measured results in transmission mode at 4.7 GHz, 6 GHz, 8 GHz, and 10.4 GHz. Measured results in reflection mode (d) at 11.7 GHz under *x*-polarized incidence, (e) at 15.4 GHz under *x*-polarized incidence, (f) at 11.7 GHz under *y*-polarized incidence, and (g) at 15.4 GHz under *y*-polarized incidence.

References

1. J. W. You, Q. Ma, L. Zhang, *et al.*, "Electromagnetic metamaterials: from classical to quantum," Electromagn. Sci. **1**, 0010051 (2023).
2. L. X. Liu, X. Q. Zhang, M. Kenney, *et al.*, "Broadband metasurfaces with simultaneous control of phase and amplitude," Adv. Mater. **26**, 5031 (2014).
3. K. B. Fan, J. Y. Suen, X. Y. Liu, *et al.*, "All-dielectric metasurface absorbers for uncooled terahertz imaging," Optica **4**, 601 (2017).
4. Z. H. Zhao, Y. Wang, C. S. Guan, *et al.*, "Deep learning-enabled compact optical trigonometric operator with metasurface," PhotoniX **3**, 15 (2022).
5. S. J. Zhang, X. Y. Chen, K. Liu, *et al.*, "Nonvolatile reconfigurable terahertz wave modulator," PhotoniX **3**, 7 (2022).
6. Z. Yue, J. T. Li, C. L. Zheng, *et al.*, "Manipulation of polarization conversion and multiplexing via all-silicon phase-modulated metasurfaces," Chin. Opt. Lett. **20**, 043601 (2022).
7. F. Aieta, P. Genevet, M. A. Kats, *et al.*, "Aberration-free ultrathin flat lenses and axicons at telecom wavelengths based on plasmonic metasurfaces," Nano. Lett. **12**, 4932 (2012).
8. K. Zhang, Y. Y. Yuan, X. M. Ding, *et al.*, "High-efficiency metalenses with switchable functionalities in microwave region," ACS Appl. Mater. Interfaces **11**, 28423 (2019).
9. R. Cacocciola, B. Ratni, N. Mielec, *et al.*, "Camouflaging a high-index dielectric scatterer with buried metasurfaces," Adv. Opt. Mater. **10**, 2101882 (2022).
10. X. W. Wang, H. Wang, J. L. Wang, *et al.*, "Single-shot isotropic differential interference contrast microscopy," Nat. Commun. **14**, 2063 (2023).
11. Z. C. Wang, G. W. Hu, X. W. Wang, *et al.*, "Single-layer spatial analog metaprocessor for imaging processing," Nat. Commun. **13**, 2188 (2022).
12. T. H. Liu, W. H. Li, Y. Y. Meng, *et al.*, "High-fidelity multiplexing metahologram for information display, storage and encryption," Mater. Des. **224**, 111353 (2022).
13. R. C. Zhu, T. S. Qiu, J. F. Wang, *et al.*, "Phase-to-pattern inverse design paradigm for fast realization of functional metasurfaces via transfer learning," Nat. Commun. **12**, 2974 (2021).
14. R. C. Zhu, J. F. Wang, C. Ding, *et al.*, "Vectorial-holography metasurface empowered by orthogonality-simplified machine learning," Mater. Des. **223**, 111273 (2022).
15. X. M. Ding, Z. C. Wang, G. W. Hu, *et al.*, "Metasurface holographic image projection based on mathematical properties of Fourier transform," PhotoniX **1**, 16 (2020).
16. Y. Li, S. Y. Chen, H. W. Liang, *et al.*, "Ultracompact multi-functional metalens visor for augmented reality displays," PhotoniX **3**, 29 (2022).

17. Y. J. Feng, Q. Hu, K. Qu, *et al.*, "Reconfigurable intelligent surfaces: design, implementation, and practical demonstration," Electromagn. Sci. **1**, 0020111 (2023).

18. T. Yan, Q. Ma, S. Sun, *et al.*, "Polarization multiplexing hologram realized by anisotropic digital metasurface," Adv. Theory Simul. **4**, 2100046 (2021).

19. R. S. Xie, Z. Gu, D. J. Zhang, *et al.*, "High-efficiency full-space complex-amplitude metasurfaces enabled by a bi-spectral single-substrate-layer meta-atom," Adv. Opt. Mater. **10**, 2102084 (2022).

20. L. Zhu, W. J. Zhou, L. Dong, *et al.*, "Full space control of meta-holograms utilizing a bilayered patterned coding metasurface," IEEE Antennas Wirel. Propag. Lett. **21**, 322 (2022).

21. L. W. Wu, H. F. Ma, Y. Gou, *et al.*, "Multitask bidirectional digital coding metasurface for independent controls of multiband and full-space electromagnetic waves," Nanophotonics **11**, 2977 (2022).

22. R. S. Xie, X. Fang, D. J. Zhang, *et al.*, "Four-channel kaleidoscopic metasurfaces enabled by a single-layered single-cell quad-band meta-atom," Adv. Theory Simul. **5**, 2100301 (2022).

23. L. Zhu, W. J. Zhou, L. Dong, *et al.*, "Meta-hologram enabled by a double-face copper-cladded metasurface based on reflection–transmission amplitude coding," Opt. Lett. **47**, 174 (2022).

24. Q. Hu, J. M. Zhao, K. Chen, *et al.*, "An intelligent programmable omni-metasurface," Laser Photonics Rev. **16**, 2100718 (2022).

25. L. Zhu, W. J. Zhou, L. Dong, *et al.*, "Multi-functional full-space metahologram employing a monolayer phase-encoding metasurface," Phys. Rev. Appl. **18**, 054080 (2022).

26. Y. Z. Cheng, W. Withayachumnankul, A. Upadhyay, *et al.*, "Ultrabroadband reflective polarization convertor for terahertz waves," Appl. Phys. Lett. **105**, 181111 (2014).